ADVANCED INTELLIGENT SYSTEMS
Open Access
www.advintellsyst.com

In-Situ Rheology Measurements via Machine-Learning Enhanced Direct-Ink-Writing

*Robert D. Weeks, Jennifer M. Ruddock, J. Daniel Berrigan, Jennifer A. Lewis, and James. O. Hardin**

Direct ink writing, an extrusion-based 3D printing method, is well suited for high-mix low-volume manufacturing. However, an iterative approach, using random selection or constant expert guidance, is still used to create printable inks and optimize printing parameters by expending significant amounts of time, materials, and effort. Herein, a machine learning (ML) model that estimates ink rheology in-situ from a simple printed test pattern is reported. This ML model is trained with a rheologically diverse set of inks composed of different polymers. The model successfully correlated features of the simple printed test pattern to rheological properties, which could, in theory, inform both printed structures and future ink compositions. The behavior of this model is verified and analyzed with explainable artificial intelligence tools, linking printed feature importance to one's known physical understanding of the process.

1. Introduction

Direct ink writing (DIW) is a widely used 3D printing technique that enables high mix, low volume (HMLV) manufacturing of lightweight architectures,[1–3] soft robotics,[4–10] and biological materials.[11,12] This broad application space makes it challenging to simultaneously optimize ink composition, rheology (e.g., viscosity, shear stress, and storage modulus), and printing parameters (e.g., nozzle size, printing pressure, and speed). Hence, considerable effort is typically required to identify target parameters for each ink used. To address these limitations, "smart" in-situ tuning of print parameters has been explored to guide filament spacing,[13–16] nozzle height,[17–20] and printing speed and pressure with the goal of reducing defects.[21,22] While these in-situ error corrections are an important step toward autonomous printing, they do not speak directly to the fluid dynamics of the print process nor guide ink formulation.

Computational fluid dynamics (CFD) models provide an alternative to an Edisonian approach to printer and ink optimization, but require knowledge of ink rheology and have primarily focused on simple Newtonian fluids.[23–27] By contrast viscoelastic inks still depend on direct measurement of their complex rheological properties using shear viscometry and oscillatory methods, which are prone to user error and challenging to automate.[28,29] Even once accurate measurements are obtained, trial and error processes are used to optimize the print parameters for a given ink to address complex behavior such as transient yielding, flow through the nozzle, and resolidification upon returning to a quiescent state. In addition, these measurements must be repeated for each ink composition formulated, limiting the manufacture of multimaterial or graded material structures.[30–32] Even minor changes in constituents used, such as polymer concentration, molecular weight, or filler content, can have pronounced effects on ink rheology. Additionally, the final behavior of the ink can depend on the conditions under which it is printed as well as time since formulation. In-situ characterization of ink rheology during DIW would facilitate improved understanding of the underlying flow physics and enable on-the-fly corrections to printing processes.

Machine learning (ML) offers powerful high throughput statistical tools that can avoid direct modeling and measurements. ML requires large data sets for model training; however the HMLV nature of DIW makes it particularly challenging to acquire large training sets due to high variability in ink properties and printed part requirements. We propose offsetting data demands by employing a simple test print pattern that is ink formulation and machine agnostic. Images of these test patterns can then be used to train a ML model, but there will still be uncertainty in the robustness and accuracy of the model due to the relatively sparse sampling of the massive DIW design space. Explainable artificial intelligence (XAI) tools provide a means of assessing the ML model and dataset for physical sensibility. Additionally, we treat our image-based ML model as a regressor

R. D. Weeks, J. A. Lewis
John A. Paulson School of Engineering and Applied Sciences
Harvard University
Cambridge, MA 02138, USA

J. M. Ruddock
UES Inc.
4401 Dayton-Xenia Rd, Dayton, OH 45432, USA

J. M. Ruddock, J. D. Berrigan, J. O. Hardin
Materials and Manufacturing Directorate
Air Force Research Laboratory
2977 Hobson Way, Wright-Patterson AFB, OH 45433-7126, USA
E-mail: james.hardin.11@afrl.af.mil

The ORCID identification number(s) for the author(s) of this article can be found under https://doi.org/10.1002/aisy.202400293.

DOI: 10.1002/aisy.202400293

for predicting rheological properties on a continuum, this has the benefit of facilitating the interpolation of new inks (and therefore new data).

Here, we demonstrate in-situ complex rheology measurements of DIW inks directly from ML-aided DIW printing, developed with the support of XAI. A set of soft viscoelastic inks with yield stress between 100 and 1,000 Pa were formulated. The ink rheology, print parameters, and test print patterns served as training data for a convolutional neural network (CNN) to predict rheology in-situ during DIW. Using a small but representative dataset, we show that a model can be trained to accurately predict the yield stress, consistency index, and flow index of inks both within the set of inks used to train the model and for new inks "unknown" to the model. To provide additional understanding, the CNN model was examined using XAI tools to identify features that strongly influence our model output. Our work provides a foundational advancement for extrusion-based 3D printing that opens new avenues for additive materials manufacturing.

2. Results

2.1. Ink Design

We hypothesize that images of a simple printed test pattern along with knowledge of corresponding printing parameters can form a meaningful estimate of ink rheology via ML-enhanced DIW (**Figure 1**). As a first step toward testing this hypothesis, we created a set of 15 inks with a representative range of rheological properties. Two material systems were used: Material System 1 (MS1) consists of 3 silicone-based inks each which are different ratios of Sylgard and SE1700 (Table S1, Supporting Information); Material System 2 (MS2) is composed of 12 acrylate-based inks, with different ratios of diurethane methylacrylate, 2-hydroxyethyl methacrylate, and fumed silica (Table S2, Supporting Information). Silicone and hydrogel inks are widely used for printing soft electronics,[33] robotics,[34,35] and shape-morphing architectures.[36,37] Each ink is characterized by oscillatory rheology to provide "Truth" data for training the ML model. Their large range of rheological properties required careful design of the rheology characterization method to give clear results for all inks. For simplicity, we used a Herschel–Bulkley (HB) fluid model (Equation (1), Figure 1a) to describe the relationship between the strain rate ($\dot{\gamma}$) and the shear stress (τ) of each ink based on three key properties: the shear yield stress (τ_γ), consistency index (k), and flow index (n).

$$\tau = \tau_\gamma + k\dot{\gamma}^n \tag{1}$$

The HB fits were reasonable for all the inks and the results can be seen in **Figure 2**a. Two material systems allow for training and testing a more generalized model, of a broader applicability for DIW. Each ink (1–15) exhibits different trends in rheological properties (Figure 2a), which are plotted in the order of increasing yield stress for each material system. For MS1 inks, their consistency index increases, while their flow index decreases with increasing shear yield stress. For MS2, the consistency index increases for each set of three adjacent inks (inks 1–3, inks 4–6, inks 7–9, and inks 10–12), corresponding to inks with the same fumed silica loading (Table S2, Supporting Information), giving the plot a "sawtooth" pattern. However, their flow index increases or remains the same within each set of inks even as the shear yield stress increases, which is markedly different than that observed for the MS1 inks. The exact

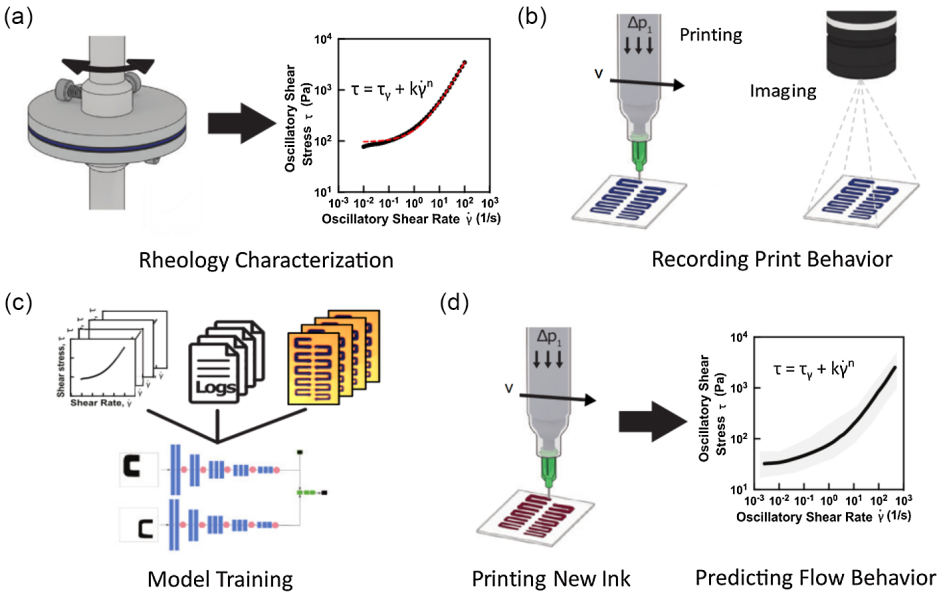

Figure 1. In-situ rheology measurements using machine learning (ML)-enhanced direct ink write. a) Characterizing ink rheology for a set of model inks on an oscillatory shear rheometer. Herschel–Bulkley model is fit to oscillatory shear rheometer measurements to extract shear yield stress, flow index, and consistency index. b) Recording print behavior for each ink in the set of model inks by printing a pattern designed to exhibit geometrical changes dependent on the fluid rheology and capturing an image of the resulting print. c) Rheology measurements, print logs, and images of printed samples are used to train a ML model. d) Print behavior is captured for a new ink and the ML model is used to predict fluid rheology.

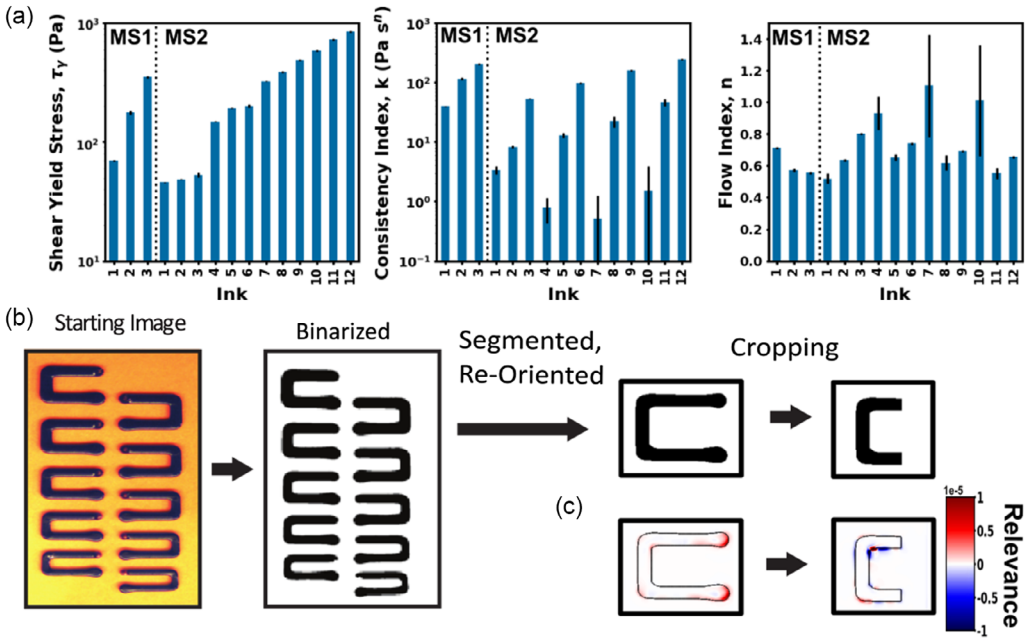

Figure 2. Dataset construction. a) Shear yield stresses, consistency indices, and flow indices for each ink. b) Image processing on starting image prior to use as model inputs. Includes cropping, glare removal, binarization, segmenting to areas of interest, mirroring C-shapes to get the same orientation, width correction and halving. c) LRP salience maps before and after halving the C-shape.

cause of this difference is beyond the scope of this work, but it is likely related to the compositions of the components of each ink system, such as molecular weight and concentration of polymers.

2.2. ML-DIW Test Pattern

We implemented a CNN-based ML model by creating a simple (2D) test pattern, collecting print data during each test print, and acquiring top-down images of each test pattern. We designed this test pattern to capture a range of flow phenomena using a minimal set of printed features (e.g., C-shaped objects) as shown in (Figure 2b). These C-shaped objects are part of a larger test pattern (see Movie S1, Supporting Information). We focused our image analysis on the C-shapes, because they contain both straight and corner segments. From the straight segments, the model can infer the approximate flow rate of each ink from the nozzle, while the local changes in nozzle speed during the corner segments enable the assessment of more dynamic behaviors. Each C-shape pattern is printed at a different printing pressure, resulting in different shear rates for a given nonlinear rheological behavior.

The dataset used for training our ML model consisted of printed test patterns and printer process logs, with rheological properties of the inks used as labels (Figure 1c). Ten test patterns are printed for each ink and then imaged resulting in a total of 150 test pattern images. Given that there are 10 C-shaped features in each test pattern, there are 1500 total C-shapes. Since each C-shape feature is printed at a different printing pressure, the toolpath is adjusted for a given pressure to minimize merging of adjacent segments within the C-shape feature. Image processing is used to adjust all images of C-shaped features to have the same distance between the arms, as shown in (Figure 2b). We hypothesized that a single top-down image of the C-shaped features in each test-pattern contains the information needed to extract critical rheological properties governing their HB flow behavior, and hence printability.

2.3. ML Model Construction and XAI

We implemented a CNN architecture based on VGG-16 due to its reliable use as an image classifier and its associated explainable AI techniques.[38–42] Our CNN is modified to both serve as a regressor and accept DIW printing pressures and C-shape images as input (**Figure 3**a). We hypothesized that each C-shape and its associated printing pressure are analogous to a single point on the rheology plot in (Figure 1a). For accurate predictions, we require more than a single C-shape/pressure pairing from a given ink. This hypothesis is explored by modifying the CNN model to accept a varying number of C-shapes and pressures in a single input. Each C-shape feature goes through the convolutional layers and then the printing pressure corresponding to each C-shape is included as an auxiliary input to the fully connected layers.

Different training/validation/test splits are used to evaluate the limitations of the dataset to interpolate (or extrapolate) for new inks or inputs. For clarity, the training set is the set of data that is optimized to minimize the mean-squared error (MSE). The MSE is an adjusted MSE calculated from the transformed dataset, described in the methods section. The trained model represents the model with the lowest MSE on the validation set. Next, we test the model on a test set to determine its final performance. The dataset splits are of two categories:

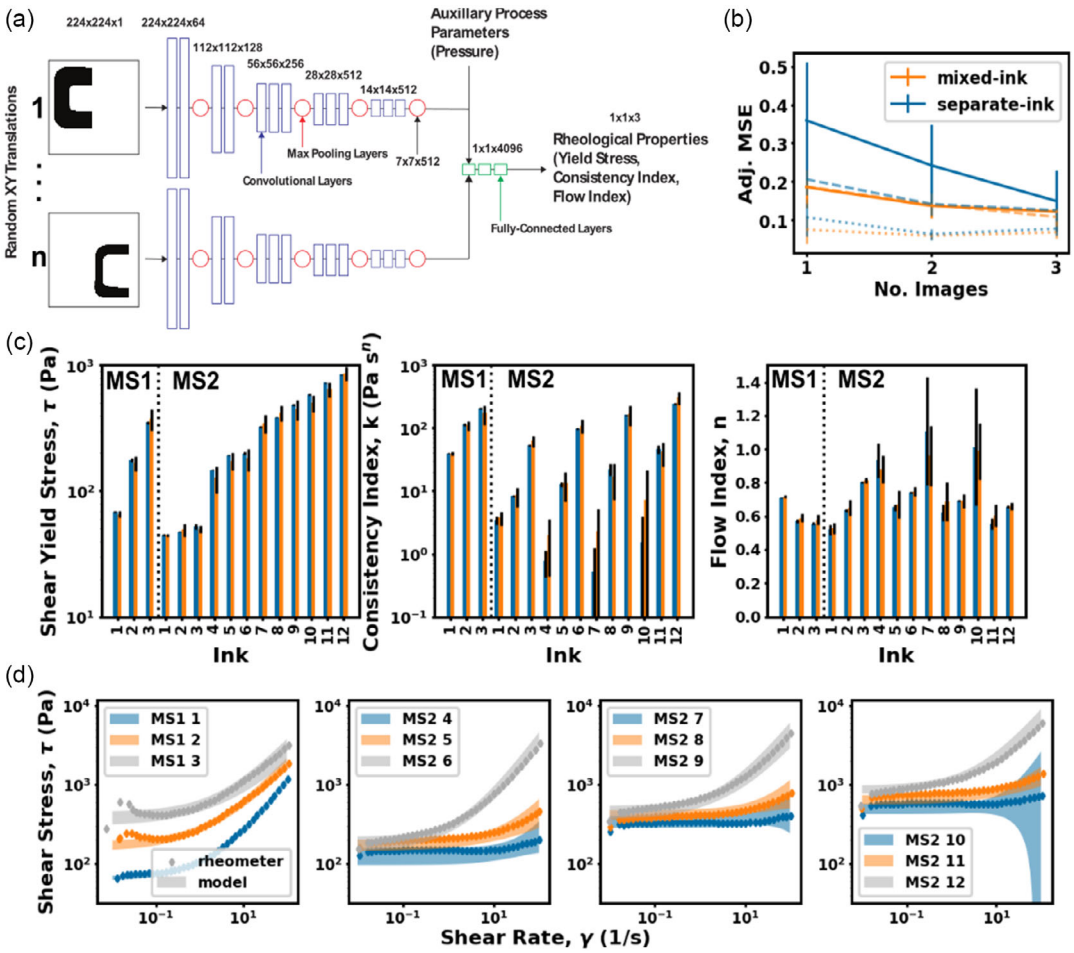

Figure 3. ML model and performance. a) Modified VGG-16 architecture for multi-image input and auxiliary pressure input. b) Errors for the different data splits for 1-image, 2-image, and 3-image inputs. Solid lines are test set errors, dashed lines are validation set errors, and dotted lines are training set errors. c) Comparison of oscillatory shear rheometer measurements to predictions from the machine learning model. d) Overlay of the model predictions (shaded region) for the Herschel–Bulkley curve on the measured stress–strain rate (dashed line) for 12 of the inks. The remaining 3 are in Figure S1, Supporting Information.

mixed-ink test set splits and separate-ink test set splits. In separate-ink test splits, all ten test patterns from each of two inks were held out as the test set. Thus, the model would be tested on C-shapes from the two inks it had never "seen". In the mixed-ink test splits, the C-shapes from 20 randomly selected test patterns were set aside for the test set. Consequently, the model would be tested on C-shapes from inks on which it had already been trained.

CNN XAI methods typically yield a "salience map" that overlays the input image, highlighting regions that most influence the CNN's decision.[43–46] To date, CNN XAI techniques used in manufacturing have been limited to defect classification models,[47–50] such as class activation mapping (CAM) to qualitatively assess the saliency in image classification of clogs in a nozzle,[47] decision tree explanations to identified images likely to be misclassified,[48] and locally-interpretable model-agnostic explanations (LIME) to find defect locations in powder bed fusion.[50] We ultimately use layerwise relevance propagation (LRP) due to its interpretability: akin to a deep Taylor decomposition, it assigns each pixel with a positive or negative contribution to the prediction.[46] This is integral to interpreting regressor results. Other advantages of LRP include the availability of open-source code and its non-reliance on perturbing inputs (i.e., "graying out" pixels) that can result in unfeasible images. LRP provides highly precise, interpretable salience maps of how a given image is influenced by the predicted rheological behavior of each ink.

2.4. Model Results

After initial training on the C-shape binary images, the LRP heatmaps (Figure 2c) shows the model placed undue attention on the ends of the C-shaped features. This region, dominated by the printing parameters (i.e., the communication and actuation delays in the pumps at the starts and stops of each C-shape feature), rather than the ink rheology. Consequently, the ends of each C-shape feature are removed (cropped off) prior to training the model. The resulting LRP heatmaps were more intuitively reasonable/robust.

Figure 3b shows the average MSE loss for models trained with different types of test-set splits and different numbers of C-image/pressure pairings per input. The training sets typically averaged around 0.07 adjusted MSE for regardless of number of C-images or dataset splitting (dotted lines). The validation error decreased from about 0.20 to 0.11 as the number of C-images per input increases (dashed lines). The test set errors for the mixed-ink split follow a similar trend to the validation error (solid orange line), and have significant overlap with the validation error lines in the plot. The highest error is seen for the test set error with a one-image input and separate-ink split, but this error dramatically decreases to approach the mixed-ink test and validation errors as the number of images increases (solid blue line). The decrease in validation and test errors with increasing the number of C-shapes per input not only indicates better performance, but also indicates less overfitting as the training error does not also decrease.

A significant change in the test set MSE is expected as more images are added as inputs. T-tests for the mixed-ink test set losses showed a significant difference between 1-image and 2-image input (p-value $= 0.0011$, $n = 30$), but no significant difference between 2- and 3-image inputs (p-value $= 0.019$, $n = 30$). The separate-ink test set losses are significantly different between 1- and 2-image inputs (p-value $= 3.2 \times 10^{-7}$, $n = 42$) and between 2- and 3-image inputs (p-value $= 3.1 \times 10^{-5}$, $n = 42$). Note, n refers to the average number of test set MSE scores. The difference in trends between the mixed- and separate-ink test sets indicates two C-shape inputs may be sufficient to identify a given ink. The low error implies that more information is available in each C-image than anticipated because at least three "points" of data are necessary to estimate the non-linear H–B curve. We posit that changes in printing speed as the nozzle is translated through the C-shape corners yields more information-rich features. On the contrary, as the number of C-shapes per input increases to three, the difference between the separate-ink and mixed-ink test errors decreases, with a p-value of 0.055 for 3-image input, implying the separate-ink error approaches the lower error observed for the mixed-ink test sets. The computational challenges of including more images coupled with the meager additional gains from additional images led to limiting the number of C-images explored to 3.

The HB property predictions for the yield stress (τ_y), consistency index (k), and flow index (n) closely follow the experimental measurements of these values obtained by oscillatory tests (Figure 3c). This is especially true for the shear yield stress, with exceptionally small standard deviations indicating a low uncertainty in those predicted values. The predicted flow behavior provides a more complete sense of the model's agreement to the measured ink rheology (Figure 3d). To our knowledge, this is the first demonstration of complex rheology predictions obtained directly from the printed test patterns.

In Figure 3c, the model predictions for the consistency index and flow index of inks 4, 7, and 10 of MS2 show significant uncertainty relative to other inks. However, we point out that the training data for these inks also had significant variability (see Figure 2a). The uncertainty in the training data could be from measurement uncertainty or fitting problems, where multiple values of fitted consistency index and flow index result in similar flow behavior. These three divergent inks have low consistency indexes and high flow indexes, as measured experimentally. While there may be a limit to the rheological range that the current model can estimate, the incorporation of additional data (training set) would likely expand this range.

2.5. Semantic XAI Analysis

To gain further insight into which data features the CNN model used to make predictions, we started with LRP salience mapping. Each LRP relevance map provides information for one input–output pairing. To gain a more comprehensive understanding of how the model works on the entire dataset, we segmented out the C-shapes into semantically relevant regions and analyzed our LRP heatmaps with respect to those regions (**Figure 4**a). To analyze the LRP images, the mean relevance value for the pixels within the vicinity of a given segment of the C-shape is recorded. This results in a transformation from the full LRP image (Figure 4a(i)) to a segment-averaged version (Figure 4a(ii)). These semantically averaged values, along with the pressure relevancies, were then used to train random forest regressors to predict the CNN's output for each of the three properties. Functionally, the random forest regressions were used to illuminate the relationship between these image features and the predicted rheological properties.

To analyze the random forest models, we calculated the permutation feature importance: the mean increase in MSE when a given feature was shuffled within the set of values of that feature in the dataset (Figure 4b). To compare our results against more standard XAI approaches, we also computed feature importances using Locally-Interpretable Model-Agnostic Explanations (LIME) and SHAPley values (SHAP) (Figure S1, Supporting Information), which corroborate the values shown in Figure 4b.[39,40] The MSE for each feature is about 0.04 before any permutations. The permutation feature importance is a statistical method calculated over 1000 iterations of shuffled features, and while every feature is included in the model, these methods do not account for feature correlations or boundary conditions. For example, the mean relevance of neighboring segments of a C-shape can also be highly correlated. These methods are not meant to be used to generate quantitative rules about the underlying physics, but rather to provide some insight into the statistical workings of the model in a qualitative sense, and link those back to the governing physics.

For the yield stress and consistency index, the pressure relevance for each C-shape is the most important feature, with the MSE increasing by 3–4 times when the pressure relevance is shuffled as seen in Figure 4b. We can see there is a fairly even distribution of lower feature importances throughout the C-shape image, however when these feature importances are summed, the total importance of the C-shape is about half the total importance of the printing pressure for both the shear yield stress and consistency index. This is not surprising for the shear yield stress, since the shear yield stress determines the minimum pressure that must be applied to each ink to initiate its volumetric flow. One would expect the consistency index to have strong relevance to both the pressure and volumetric flow rate, partially indicated by the image data. In this experiment,

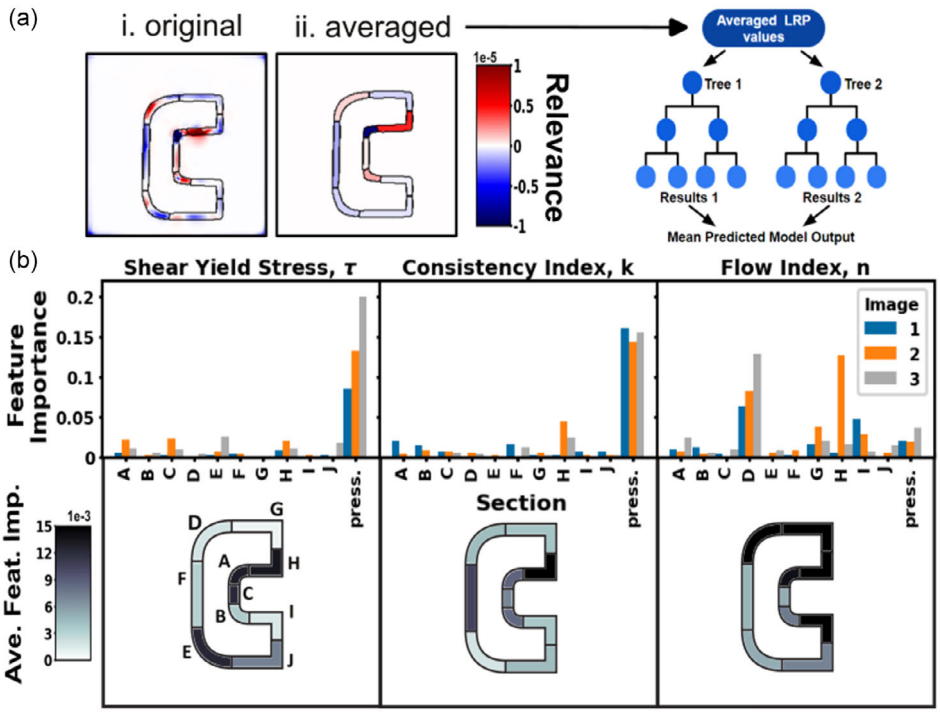

Figure 4. Explainable AI. a) Layerwise Relevance Propagation (LRP) analysis. i. Original LRP saliency map for a single input image. ii. Segment-averaged LRP saliency map. These values are used as random forest input to predict the CNN output. b) Permutation feature importances on the test set averaged over 1000 iterations showing importance of image areas and pressures. The C-shape segments are labeled A-J as shown, and the average feature importance for each segment across the 3-image in is shown using a colormap.

manually picking a pressure for each ink that extrudes at approximately the same volumetric flow rate likely results in the pressure value having a higher relevance to the consistency index than one would initially expect. In contrast, the XAI identifies more feature importance throughout the C-shape and less on the printing pressure for the flow index. The flow index affects the shear-thinning of the inks, significantly affecting the dynamic flow behavior while extruding around the bends in the C-shapes. Here, the summed feature importances for the C-shape is about ten times greater than the summed feature importances for the pressure.

3. Conclusion

In summary, we have demonstrated the application of ML-enhanced DIW to directly determine ink rheology from a simple printed pattern. Our model not only captures the rheological behavior of known inks but is reasonably effective at predicting the properties of new inks. By coupling the model with XAI tools, the model could rapidly assess which data features were important for predicting a given rheological property. These identified features could then be linked back to the direct ink writing process to ensure that the model was "focused" on intuitively reasonable features. This advance represents an important step toward autonomous 3D printing, in which printers are capable of creating new inks and optimizing print parameters on-the-fly without human intervention.

4. Experimental Section

Ink Preparation: The silicone inks are prepared by mixing three different ratios of Dowsil SE 1700 (Dow) to Sylgard 184 (Dow) (see Table S1, Supporting Information). The acylate inks are formulated from three components, diurethane dimethacrylate (Millipore Sigma), 2-hydroxyethyl methacrylate (HEMA, Millipore Sigma) and fumed silica (CAB-O-SIL TS-720, Cabot) in varying proportions (see Table S2, Supporting Information). All inks are prepared in the same manner. The fumed silica is added in 0.2 g increments. Following the addition of fumed silica, the components are thoroughly mixed in a planetary mixer (FlackTeK SpeedMixer) at 800 rpm for 30 s, 1600 rpm for 30 s and 2200 rpm for 3 min. The addition of fumed silica and the mixing cycle is repeated until the final total fumed silica content is reached. Finally, 0.2 g of blue pigment (Silc Pig, Smooth-OnSmooth-On) is added for color. The inks are then loaded into 10 cc syringe barrels (Nordson EFD) and centrifuged at 4000 rpm for 3 min to remove any air entrapped in the barrel.

Rheological Characterization: The rheology of the inks is measured using a rotational rheometer (Discovery HR-20 hybrid rheometer; TA Instruments). Three oscillatory shear stress (τ) measurements are carried out for each ink under direct strain control at room temperature (21 °C) using a 40 mm diameter disposable parallel plate geometry with 120 grit sandpaper and a 500 µm gap. A conditioning step is first applied to the sample, consisting of a preshear at a rate of 1.0 s^{-1} for 20 s, followed by 120 s of equilibration time. Oscillatory measurements are captured using a sweep of angular frequencies from 0.01 rot/s to 100 rot/s (0.0628 rad s^{-1} to 628.0 rad s^{-1}) at 16% strain

Printing System: The printing system consists of: the motion-controlled three-axis stage, the printhead, the sensor array, the alignment system, and software. The cartesian motion stage (customized ABG 1000, Aerotech Inc.) features 4 parallel independently controlled z-axes. The printhead is affixed to the first of these axes and consists of a syringe with

a 0.84 mm (18 gauge) inner diameter 0.5" long straight stainless-steel nozzle (Nordson EFD) connected to an electronic pressure regulator (Ultimus V, Nordson EFD) to control extrusion. The electronic pressure regulator is connected over serial (RS-232) to the controller of the motion stage (A3200, Aerotech Inc.). The sensor array is affixed to a second z-axis. The array consists of a downwards facing camera (IDS UI-325°CP with Tamron M118FM16 lens) and a contact-type digital displacement sensor (HG-S1110-AC, Panasonic) pneumatically actuated through a second electronic pressure regulator (Ultimus V, Nordson EFD) and connected by digital signal to the motion stage controller (A3200, Aerotech Inc.). The alignment system consists of three optical micrometers (LS-7010, Keyence) mounted to custom machined fixtures and connected over RS-232 to the motion stage controller (A3200, Aerotech Inc.). A $50 \times 75 \times 1$ mm uncoated glass slide is used as the printing substrate and held in place with a laser cut acrylic fixture. The digital displacement sensor is used to probe 9 positions on the glass slide to create a heightmap used to ensure accurate nozzle height during the print. A laser cut orange cardstock is used as a contrasting background behind the glass slide. A base pressure for each ink is determined by manually adjusting the pressure supplied to the syringe barrel until ≈160 mg of ink are extruded over the course of 30 s. This extrusion rate ensured that 2 mm s^{-1} translation speeds while printing were appropriate. Positional data was collected at 1 kHz to facilitate future adaptations to printers with different acceleration profiles. Open source Python automation software, APE,[51] was used to coordinate the other components of the printing system and collect the associated data

Image Processing: The portion of the test print image that contained the 10 C-shaped features was identified using matchTemplate from OpenCV with an ideal C pattern image at various scaling.[52] This section contained only 10 C-shaped features with a background of the slide alone. Pixels were then sorted into background and ink using k-means (Scikit-Learn) on the RGB values.[53] Pixels were assigned to ink if they were much closer to the ink centroid from the k-mean analysis than the background centroid. This assignment was used to generate a binary representation of the C-shaped features. Glare was removed on the binarized image using MORPH_CLOSE with the number of iterations that best remove small glare regions while still retaining the original shape. C-shapes were then rotated, bisected at the midline to remove the ends. The distance between the two "arms" of the C-shape corrected by identifying the center axis of the C-shape and the center-lines of the 2 "arms", relocating two "arms" to the same distance apart, and extending the "bend" in the C-shape from one arm to the next

Machine Learning: Machine Learning was performed with the built-in VGG-16 network of PyTorch's Torchvision module, modified with Leaky ReLU activation functions and to take in a variable number of C-shape inputs.[38,54] The data input was modified before entering the model: the binarized images were converted to pixel values of −0.5 and 0.5. Each image would pass through the convolutional layers before being flattened and concatenated into the fully connected layers. The images were augmented by random translation using Torchvision's transforms. RandomAffine() method. The maximum horizontal translation was 55 pixels, while the maximum vertical translation was 21, such that at no point would any C-shape not be fully in the image. The RandomAffine arguments for rotation, shear, and rescaling were not used. Rather than creating a larger dataset using a fixed set of randomly translated images, which would result in the need for more storage and in overfitting to the training set, the images were randomly translated on-the-fly. This helped minimize overfitting, and mitigated any effect the proximity of the c-shape edges to the edges of the image would have on the output. Other augmentation methods such as flips and rotations or rescaling the c-shapes resulted in poorer fits. No methods that involved distortion of the C-shape were attempted, due to the importance of the shape of the C on the output

The pressures that each C-shape were printed at were also concatenated with the flattened convolutional outputs as an auxiliary input. The pressure (in PSI), covered several orders of magnitude so was log-transformed and centered around zero before using the formula $P' = (\log(P) - 3.1)/2$. The yield stress and consistency index each cover several orders of magnitude, so those two properties were log transformed before training. In addition, the three properties were all rescaled and centered, such that they each had a similar range of values and no one property would dominate the error. This process is performed *ad hoc* and may need to be adjusted as more inks are added to the dataset. Thus, the resultant formulas are $\tau' = \log(\tau) - \log(\min(\tau)))/1.2$ for the adjusted yield stress, $k' = (\log(k) - \log(\min(k)))/2.2$ for the adjusted consistency index, $n' = (n - \min(n))*4.2$ for the adjusted flow index, with τ in MPa, k in MPa*s^n, and min(x) being the minimum value across the entire dataset (all 15 inks) rounded down to the nearest hundredth.

The models were trained with an Adam optimizer and a mean-squared error loss function. For mixed-ink testing, the 150 tiles were randomly divided 80:50:20 into training:validation:test sets. he average test errors for models trained on 10 different training:validation:test sets were used. For separate-ink testing, 2 inks were chosen as test inks, and the other 130 tiles were randomly divided 80:50 into the training and validation set. There are 105 possible 2-ink combinations for the separate-ink test set. To make sure we had meaningful test sets, we chose 2-ink combinations that were not neighboring each other in value for any of the 3 properties. Due to the lack of prediction accuracy with inks 4, 7, and 10 of MS2, they were also not included in any of the separate-ink test sets.

For the different numbers of image inputs, each tile would be randomly divided into groups of 1-, 2- or 3-images. In the case of the 3-image input, each tile would provide 3 3-image inputs while one C-shape went unused. Grid-search hyperparameter tuning was performed to find the best number of image inputs, learning rate, and weight decay, resulting in a learning rate of 1×10^{-4} and weight decay of 1×10^{-5}. Dropout was included during the hyperparameter tuning of the first 2 fully-connected layers of the CNN, with a probability of 0.5 of an element in those layers being zeroed. The training and hyperparameter tuning were tracked with Weights and Biases.[55]

Explainable AI: The LRP code is based on tutorial code from Montavon et al.[46] The z^B-rule used for the input layer was modified for the binarized image input. The binarized pixels of the input images had a value of either −0.5 or 0.5, so the lower and upper bounds were changed to −0.501 and 0.501. Furthermore, because the activation functions were changed from ReLu to LeakyReLu, negative activations were factored by 0.01 before proceeding through the backward propagating the relevance. Other modifications for the three-image input and auxiliary inputs were superficial, simply adding steps for propagating through each image, and adding and removing the auxiliary inputs so they are only processed in the fully connected layers.

Different regions of the C-shape were labeled by segmenting out the edges. The edges of each C-shape image were found using a canny edge filter. The sides of the top and bottom filaments are found using a k-means clustering algorithm (scikit-learn) on the locations of the edges along the right side of the C-shape.[53] The center of the inner bend was identified as the rightmost edge between the two arms. The upper inner corner was then guessed as being in the edge from the inner bend to the lower edge of the top filament (Figure S3, Supporting Information). This region would contain section A (the upper inner corner) but also some of sections C and H. Then straight edges of sections C and H in the region are then removed until the edge contains just section A, with straight segments no longer than ten pixels. The analogous process was done for the lower inner corner, and for the outer corners using the outer bend as a starting point. From there, the straight segments that are not part of the corners are labeled.

Semantic meaning is assigned by taking the labeled C-shape outline as described in the previous paragraph and making it thicker with the binary-dilation method while keeping the labels associated with the nearest section. Then for each section of the c-shape, the mean of the pixels of the LRP relevance map that overlay that section is recorded. These mean values, along with the relevance of the pressure inputs, are used as data for a random forest regressor (Scikit-Learn),[53] with the output property as the labels. The random forest was trained with 8-fold cross-validation on the training set used to train the CNN. The tuned hyperparameters were the number of features to consider when choosing a split, and the number of trees used in the forest. Random Forest was chosen because it is quick, and pulling the feature importances out of it is straightforward using the

sklearn.inspection API. The permutation feature importance was calculated on the test dataset over 1000 iterations. LIME and SHAPley explanations were calculated for 40 randomly chosen samples (Figure S1, Supporting Information) using the LIME and DALEX python software packages.[44,45,56] In addition to the random forest regressor we also tried more direct analysis but correlations between outputs and the mean LRP values were small, with Pearson correlations varying between −0.2 and 0.2. Simple linear regression, principal component analysis, and manifold learning techniques also proved fruitless.

Supporting Information

Supporting Information is available from the Wiley Online Library or from the author.

Acknowledgements

R.D.W. and J.M.R. contributed equally to this work. The authors would like to acknowledge Ezra Ameperosa for assistance with CNN development and Nicolas Arn for image analysis code support. This work was funded by AFRL/RXM Core funding and the NSF through the Harvard Materials Research Science and Engineering Center (MRSEC; DMR-2011754). The authors gratefully acknowledge support from the Army Research Office MURI Program (grant no. W911NF2120146).

Conflict of Interest

J.A.L. is a member of the Scientific Advisory Boards of Azul3D and Desktop Metal.

Author Contributions

James. O. Hardin: Conceptualization:Equal; Data curation:Equal; Formal analysis:Supporting, Investigation:Lead, Investigation:Lead, Investigation: Lead; Validation:Supporting; Visualization:Lead; Writing—original draft:Lead; Writing—review and editing:Equal. **Robert D. Weeks:** Conceptualization:Equal; Conceptualization:Equal; Formal analysis: Supporting; Investigation:Lead; Methodology:Equal; Software:Supporting; Validation:Supporting; Visualization:Lead; Visualization:Lead; Writing—review and editing:Equal. **Jennifer M. Ruddock:** Conceptualization: Supporting; Data curation:Equal; Formal analysis:Lead; Investigation: Equal; Methodology:Equal; Software:Equal; Validation:Lead; Visualization: Equal; Writing—original draft:Lead; Writing—review and editing:Lead. J. **Daniel Berrigan:** Conceptualization:Supporting; Funding acquisition:Lead; Resources:Equal; Writing—review and editing:Supporting. **Jennifer A. Lewis:** Conceptualization:Supporting; Data curation:Supporting; Methodology:Supporting; Resources:Equal; Supervision:Supporting; Validation:Supporting; Writing—original draft:Supporting; Writing—review and editing:Equal.

Data Availability Statement

The data that support the findings of this study are available from the corresponding author upon reasonable request.

Keywords

3D printing, artificial intelligence, explainable artificial intelligence, machine learning, rheology

Received: April 19, 2024
Published online:

[1] B. G. Compton, J. A. Lewis, *Adv. Mater.* **2014**, *26*, 5930.
[2] J. Mueller, J. R. Raney, K. Shea, J. A. Lewis, *Adv. Mater.* **2018**, *30*, 1705001.
[3] V. C.-F. Li, C. K. Dunn, Z. Zhang, Y. Deng, H. J. Qi, *Sci. Rep.* **2017**, *7*, 8018.
[4] R. R. Kohlmeyer, A. J. Blake, J. O. Hardin, E. A. Carmona, J. Carpena-Núñez, B. Maruyama, J. Daniel Berrigan, H. Huang, M. F. Durstock, *J. Mater. Chem. A* **2016**, *4*, 16856.
[5] A. J. Blake, R. R. Kohlmeyer, J. O. Hardin, E. A. Carmona, B. Maruyama, J. D. Berrigan, H. Huang, M. F. Durstock, *Adv. Energy Mater.* **2017**, *7*, 1602920.
[6] K. Sun, T.-S. Wei, B. Y. Ahn, J. Y. Seo, S. J. Dillon, J. A. Lewis, *Adv. Mater.* **2013**, *25*, 4539.
[7] B. Y. Ahn, E. B. Duoss, M. J. Motala, X. Guo, S.-I. Park, Y. Xiong, J. Yoon, R. G. Nuzzo, J. A. Rogers, J. A. Lewis, *Science* **2009**, *323*, 1590.
[8] A. D. Valentine, T. A. Busbee, J. W. Boley, J. R. Raney, A. Chortos, A. Kotikian, J. D. Berrigan, M. F. Durstock, J. A. Lewis, *Adv. Mater.* **2017**, *29*, 1703817.
[9] T. J. Wallin, J. Pikul, R. F. Shepherd, *Nat. Rev. Mater.* **2018**, *3*, 84.
[10] A. Kotikian, C. McMahan, E. C. Davidson, J. M. Muhammad, R. D. Weeks, C. Daraio, J. A. Lewis, *Sci. Rob.* **2019**, *4*, eaax7044.
[11] S. C. Altıparmak, V. A. Yardley, Z. Shi, J. Lin, *J. Manuf. Proc. 2022*, *83*, 607.
[12] I. Ianovici, Y. Zagury, I. Redenski, N. Lavon, S. Levenberg, *Biomaterials* **2022**, *284*, 121487.
[13] J. Plott, A. Shih, *Addit. Manuf.* **2017**, *17*, 1.
[14] X. Tian, Y. Li, D. Ma, J. Han, L. Xia, in *Proc. ASME 2021 16th Int. Manufacturing; Science and Engineering Conference. Volume 1: Additive Manufacturing; Advanced Materials Manufacturing; Biomanufacturing; Life Cycle Engineering; Manufacturing Equipment and Automation*, ASME, Virtual, Online, **2021**, V001T01A019.
[15] E. Shojaei Barjuei, E. Courteille, D. Rangeard, F. Marie, A. Perrot, *Adv. Ind. Manuf. Eng.* **2022**, *5*, 100094.
[16] P. F. Yuan, Q. Zhan, H. Wu, H. S. Beh, L. Zhang, *J. Build. Eng.* **2022**, *46*, 103716.
[17] Z. Jin, Z. Zhang, G. X. Gu, *Adv. Intell. Syst.* **2020**, *2*, 1900130.
[18] Z. Jin, Z. Zhang, G. X. Gu, *Manuf. Lett.* **2019**, *22*, 11.
[19] S. G. M. Uzel, R. D. Weeks, M. Eriksson, D. Kokkinis, J. A. Lewis, *Adv. Mater. Technol.* **2022**, *7*, 2101710.
[20] Z. Zhu, S.-Z. Guo, T. Hirdler, C. Eide, X. Fan, J. Tolar, M. C. McAlpine, *Adv. Mater.* **2018**, *30*, 1707495.
[21] W. J. Wright, J. Darville, N. Celik, H. Koerner, E. Celik, *Addit. Manuf.* **2022**, *58*, 102985.
[22] M. V. Johnson, K. Garanger, J. O. Hardin, J. D. Berrigan, E. Feron, S. R. Kalidindi, *Addit. Manuf.* **2021**, *46*, 102191.
[23] R. Comminal, M. P. Serdeczny, D. B. Pedersen, J. Spangenberg, *Addit. Manuf.* **2018**, *20*, 68.
[24] R. Comminal, M. P. Serdeczny, D. B. Pedersen, J. Spangenberg, *Addit. Manuf.* **2019**, *29*, 100753.
[25] J. Göhl, K. Markstedt, A. Mark, K. Håkansson, P. Gatenholm, F. Edelvik, *Biofabrication* **2018**, *10*, 034105.
[26] Y. Tu, A. Hassan, J. A. Arrieta-Escobar, U. K. U. Zaman, A. Siadat, G. Yang, *Int. J. Adv. Manuf. Technol.* **2022**, *120*, 3821.
[27] Y. Tu, A. Hassan, A. Siadat, G. Yang, Z. Chen, *Int. J. Adv. Manuf. Technol.* **2022**, *123*, 599.
[28] C. Clasen, P. M. Phillips, L. Palangetic, J. Vermant, *AIChE J.* **2012**, *58*, 3242.

[29] R. H. Ewoldt, M. T. Johnston, L. M. Caretta, in *Complex Fluids in Biological Systems* (Ed.: S. E. Spagnolie), Springer, New York, NY **2015**, Experimental Challenges of Shear Rheology: How to Avoid Bad Data.
[30] T. J. Ober, D. Foresti, J. A. Lewis, *Proc. Natl. Acad. Sci. USA* **2015**, *112*, 12293.
[31] J. M. Ortega, M. Golobic, J. D. Sain, J. M. Lenhardt, A. S. Wu, S. E. Fisher, L. X. Perez Perez, A. W. Jaycox, J. E. Smay, E. B. Duoss, T. S. Wilson, *Adv. Mater. Technol.* **2019**, *4*, 1800717.
[32] B. Duncan, R. D. Weeks, B. Barclay, D. Beck, P. Bluem, R. Rojas, M. Plaut, J. Russo, S. G. M. Uzel, J. A. Lewis, T. Fedynyshyn, *Adv Mater. Technol.* **2023**, *8*, 2201496.
[33] J. M. Morales Ferrer, R. E. Sánchez Cruz, S. Caplan, W. M. van Ross, J. W. Boley, *Adv. Mater.* **2024**, *36*, 2470061.
[34] R. L. Truby, J. A. Lewis, *Nature* **2016**, *540*, 371.
[35] R. L. Truby, M. Wehner, A. K. Grosskopf, D. M. Vogt, S. G. M. Uzel, R. J. Wood, J. A. Lewis, *Adv. Mater.* **2018**, *30*, 1706383.
[36] A. S. Gladman, E. A. Matsumoto, R. G. Nuzzo, L. Mahadevan, J. A. Lewis, *Nat. Mater.* **2016**, *15*, 413.
[37] J. W. Boley, W. M. van Rees, C. Lissandrello, M. N. Horenstein, R. L. Truby, A. Kotikian, J. A. Lewis, L. Mahadevan, in *Proc. Natl. Acad. Sci. USA* **2019**, *116*, 20856.
[38] K. Simonyan, A. Zisserman,in Int. Conf. on Learning Representations, San Diego, CA, USA 2015, Very Deep Convolutional Networks for Large-Scale Image Recognition.
[39] T. Kaur, T. K. Gandhi, in *Int. Conf. Information Technology (ICIT)*, IEEE, Bhubaneswar, India **2019**, p. 94.
[40] S. Mascarenhas, M. Agarwal, in *2021 Inter. Conf. Disruptive Technologies for Multi-Disciplinary Research and Applications (CENTCON)*, IEEE, Bengaluru, India **2021**, p. 96.
[41] H. Wang, in *2020 3rd Inter. Conf. Advanced Electronic Materials, Computers and Software Engineering (AEMCSE)*, IEEE, Shenzhen, China **2020**, p. 252.
[42] S. Islam, S. I. A. Khan, Md. M. Abedin, K. M. Habibullah, A. K. Das, in *Proc. 2019 7th Int. Conf. Computer and Communications Management*, ACM, New York **2019**, p. 38.
[43] R. R. Selvaraju, A. Das, R. Vedantam, M. Cogswell, D. Parikh, D. Batra, *Int. J. Comput. Vision* **2019**, *128*, 336.
[44] M. T. Ribeiro, S. Singh, C. Guestrin, in *Proc. 22nd ACM SIGKDD Inter. Conf. Knowledge Discovery and Data Mining*, ACM, New York, NY **2016**, 1135.
[45] E. Štrumbelj, I. Kononenko, *Knowl. Inf. Syst.* **2014**, *41*, 647.
[46] G. Montavon, A. Binder, S. Lapuschkin, W. Samek, K.-R. Müller, in *Explainable AI: Interpreting, Explaining And Visualizing Deep Learning*, Springer Nature Switzerland AG, Cham, CH **2019**, Ch. 10.
[47] M. Lee, J. Jeon, H. Lee, *J. Intell. Manuf.* **2022**, *33*, 1747.
[48] A. B. Chu, M. Murialdo, J. P. Lewicki, J. N. Rodriguez, M. K. Shiflett, B. Giera, A. D. Kaplan, in *2019 18th IEEE Int. Conf. Machine Learning and Applications (ICMLA)*, IEEE, Piscataway, NJ **2019**, p. 1342.
[49] S. Meister, M. Wermes, J. Stüve, R. M. Groves, *Compos. Part B: Eng.* **2021**, *224*, 109160.
[50] A. Pratap, N. Sardana, S. Utomo, A. John, P. Karthikeyan, P.-A. Hsiung, in *2023 15th Inter. Conf. Knowledge and Smart Technology (KST)*, Phuket, Thailand **2023**, p. 1.
[51] J. O. Hardin, *APE* **2020**, https://github.com/jhardin4/APE.
[52] G. Bradski, *Dr. Dobb's J. Software Tools* **2000**, 2236121.
[53] F. Pedregosa, G. Varoquaux, A. Gramfort, V. Michel, B. Thirion, O. Grisel, M. Blondel, P. Prettenhofer, R. Weiss, V. Dubourg, J. Vanderplas, A. Passos, D. Cournapeau, M. Brucher, M. Perrot, E. Duchesnay, *J. Mach. Learning Res.* **2011**, *12*, 2825.
[54] A. Paszke, S. Gross, F. Massa, A. Lerer, J. Bradbury, G. Chanan, T. Killeen, Z. Lin, N. Gimelshein, L. Antiga, A. Desmaison, A. Kopf, E. Yang, Z. DeVito, M. Raison, A. Tejani, S. Chilamkurthy, B. Steiner, L. Fang, J. Bai, S. Chintala, in *Advances Neural Inf. Proc. System* (Eds: H. Wallac, H. Larochelle, A. Beygelzimer, F. d'Alché-Buc, E. Fox, R. Garnett) 2019, Vol. *32* NeurIPS, Vancouver, CA **2019**, PyTorch: An Imperative Style, High-Performance Deep Learning Library.
[55] L. Biewald, *Experiment Tracking with Weights and Biases* **2020**, http://wandb.com/.
[56] P. Biecek, T. Burzykowski, *Explanatory Model Analysis*, Chapman and Hall, CRC New York **2021**.